



Generation mechanism of surface micro-texture in axial ultrasonic vibration-assisted milling (AUVAM)

Zongbo Zhang¹ · Wengang Liu¹ · Xintong Chen¹ · Yu Zhang¹ · Chunling Xu¹ · Kai Wang¹ · Wei Wang¹ · Xin Jiang¹

Received: 23 May 2022 / Accepted: 14 August 2022 / Published online: 24 August 2022
© The Author(s), under exclusive licence to Springer-Verlag London Ltd., part of Springer Nature 2022

Abstract

Although axial ultrasonic vibration-assisted milling (AUVAM) is promising for rapid and economical fabrication of 3D micro-texture on various surfaces, it has been a challenge to obtain micro-texture with small feature size and large height simultaneously. The mechanism and major influence factors for the formation of micro-texture by this method were explored in this study. It was found that the generation of micro-texture was mainly caused by cutting and extrusion from the flank face of the milling tool under ultrasonic vibration. Therefore, a novel 3D tool model that considered the relief angle, end cutting edge angle and the blade profile was established in simulation analysis. The good agreement between simulation and experimental results demonstrated that the influence of the flank face on the micro-texture was mainly attributed to the relief angle of the milling tool. It was the first time to report that both the height and the profile shape of the micro-texture unit were affected by the overlap and extrusion between the flank surface and the micro-texture. But this influence diminished with the increase of spindle speed. 3D sinusoid-shaped micro-texture with minimum width of 20 μm and height of 2 μm (fully reproduced the ultrasonic amplitude) was realized with the relief angle of 40° and spindle speed of 4000 rpm. Other typical textures of weave, shell, scale and corrugation were also presented to show the effective regulation of texture patterns in AUVAM. This work provides both theoretical and practical basis for such a low-cost, efficient and controllable 3D micro-texture preparation method.

Keywords Axial ultrasonic vibration-assisted milling (AUVAM) · Micro-texture · Generation mechanism · Relief angle · Spindle speed

1 Introduction

Micro-textured surface has been widely used in the fields of optics [1–3], biomedicine [4–6] and mechanical engineering [7, 8] due to its diverse applications in self-cleaning [9], drag and friction reduction [10, 11]. Along with the increasing demands of micro-textured surface in industry, various artificial manufacturing technologies have arisen, such as reactive ion etching (RIE) [12], lithographic galvanofornung abformung (LIGA) [13], laser surface texturing (LST) [14] and electrochemical technology [15]. However, most of the above-mentioned methods are not competent for large-scale production owing to their disadvantages of expensive

equipment or cumbersome process. In contrast, ultrasonic-assisted traditional machining technology [16] is a potential method to overcome the above-mentioned problems, by which rapid and low-cost fabrication of micro-texture can be realized.

Milling has been proven to be one of the most competent traditional machining methods due to its advantages in efficiency, applicability and stability. Ultrasonic vibration-assisted milling (UVAM) [17–20] is a non-traditional machining method, which exerts extra high-frequency vibration on tool or workpiece during milling process. Ultrasonic vibration-assisted mechanisms are designed to excite ultrasonic vibrations, and the core component is the transducer [21, 22]. Feng et al. [23–27] carried out a systematic study of UVAM, which theoretically explained the mechanism of improving machining quality and reducing cutting force. Particularly, micro-texture possessing specific function can also be achieved by UVAM. Shen and Tao [28] fabricated micro-texture on

✉ Zongbo Zhang
zzb001_0@163.com

¹ College of Mechanical and Electrical Engineering, China University of Petroleum (East China), Qingdao 266580, People's Republic of China

aluminum alloy surface using UVAM and demonstrated great improvement in lubricant absorption and reservation capacity. Chen et al. [11] machined textures on the surface of CuAlNi by UVAM and showed superior fretting wear performance of the surface. Micro-textures [29] were obtained on aluminum alloy surface to successfully improve and control the wettability of the surface. As UVAM shows promising prospect for the preparation of micro-texture, it has attracted wide attention in recent years. However, most researchers exerted the ultrasonic vibration in the feed or cutting direction (perpendicular to the tool axis). Based on this method, Chen et al. [30] fabricated fish scales and wave-textured surfaces with a height of less than 2 μm under the ultrasonic amplitude of 7 μm . Shen et al. [31] realized three texture patterns, which were rib, scale and wave, at different spindle speeds by the analysis of tool tip trajectory. The maximum height of the micro-texture was around 1 μm , while the ultrasonic amplitude was 7 μm . Lu et al. [32] designed ripple and fish scale textures by analytical calculation and fabricated them in experiment. Although the ultrasonic amplitude was up to 10 μm , the height of these textures was around 2 μm . All the above studies focused on the fabrication of planar patterns, resulting from the tool trajectory during UVAM. In this process, the pattern shape and feature width of the micro-texture were determined by the ultrasonic amplitude and frequency. But the height of micro-texture cannot be tuned by ultrasonic vibration. Consequently, it is infeasible to realize complex 3D textures with great height by this kind of UVAM method.

In the past few years, some researchers exerted the ultrasonic vibration in tool axis direction, which termed AUVAM. Börner et al. [33] studied the fabrication of micro-texture on cold-working steel surface by AUVAM. The results illustrated that the height of the micro-texture could be effectively controlled by the amplitude of the ultrasound. Micro-textures with the height of 4 μm and width of 100 μm were achieved under the ultrasonic amplitude of 4 μm . Although the amplitude of the ultrasonic vibration was fully reproduced onto the height of the micro-texture in this study, the feature size (100 μm) was too large for most applications. Zhao et al. [34] studied on the fabrication of micro-texture with smaller feature size by AUVAM. Uniform micro-texture with a height of 1 μm and a width of 15 μm was obtained under the ultrasonic amplitude of 2 μm . It was found that the micro-textured height diminished with the decrease of the feature size under a certain amplitude of ultrasound. The above studies implied that the height of micro-texture could be regulated by the ultrasonic amplitude. And complex 3D texture can also be theoretically achieved by precisely controlling the height of the texture. However, the reproduction of the ultrasonic amplitude onto the height of the micro-texture is a common problem,

especially for textures with small feature size. Until now, the reason for this problem and the effective regulation of the texture height during AUVAM have never been reported.

In this paper, the generation mechanism of micro-texture and the main influence factors of its height and profile shape in AUVAM were explored by theoretical and simulation analysis. Theoretical deduction revealed that the relief angle and spindle speed of the milling tool significantly affected the profile of micro-texture. On this basis, a 3D tool model considering relief angle, end cutting edge angle and blade profile was established in simulation. The influence of relief angle and spindle speed of the tool on the height and profile shape of micro-texture were studied by simulation and experiment. Micro-texture with the minimum width of 20 μm and height of 2 μm (fully reproduced the ultrasonic amplitude) was obtained. Moreover, the regulation of micro-textured surface was explored by changing the processing parameters and the relief angle of the milling tool.

2 Surface texture generation mechanism of AUVAM

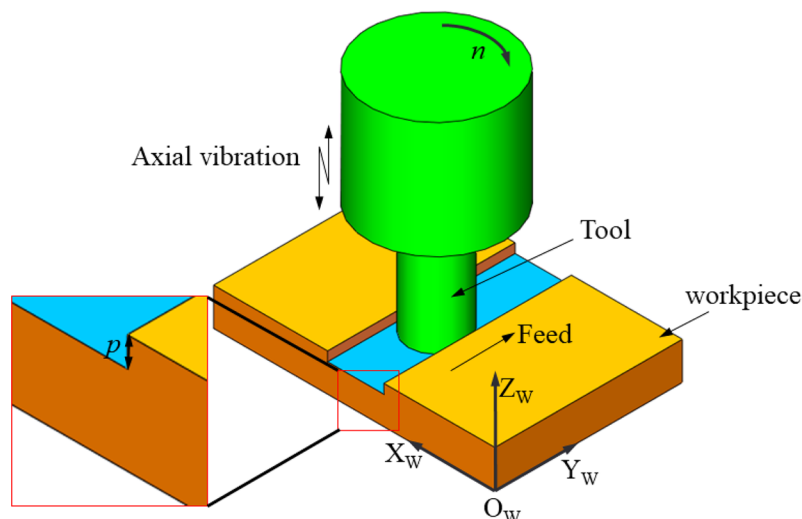
2.1 Theory analysis

Figure 1a shows the schematic of the AUVAM process. The tool rotates with the spindle speed n around Z axis. The spindle moves in a straight line along the Y axis with the feed per tooth (FPT) of f_z . The tool vibrates with the amplitude A along the Z axis at the ultrasonic vibration frequency f . Consequently, the tool trajectory is a 3D sinusoidal periodic oscillation curve in space as shown by the red line in Fig. 1b, which is quite different from traditional milling (blue line) or UVAM (green line). Moreover, the preset cutting depth p is normally much greater than the vibration amplitude A . Therefore, the material is continuously removed from the workpieces during the machining process.

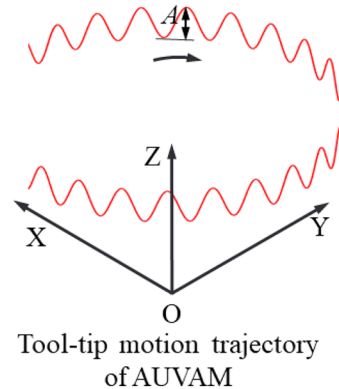
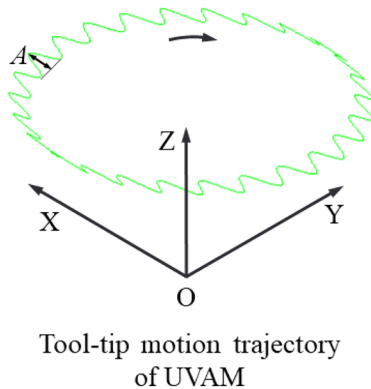
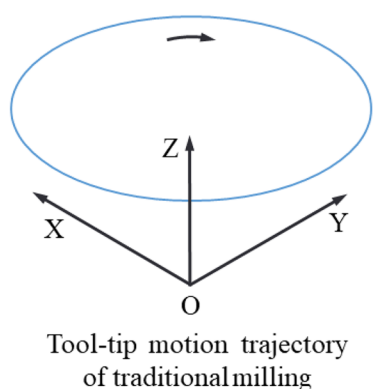
According to the coordinate system in Fig. 2a, the trajectory of tool tip that changes with time t can be expressed as follows:

$$\begin{cases} x = R\sin\theta_t \\ y = R\cos\theta_t + 2f_z nt \end{cases} \quad (1)$$

where R is the radius of milling tool (μm), n is the spindle speed (rpm), t is the machining time (s), θ_t is the rotation angle of the tool tip (rad). When the ultrasonic vibration with certain amplitude and frequency is imposed in the axial direction, the trajectory changes in the Z direction, as shown in Fig. 2b. And the trajectory change in the Z direction within the period time t can be written as:



(a)



(b)

Fig. 1 Schematic diagram of the AUVAM process: a the process of AUVAM; b tool tip trajectory of different milling processes

$$\begin{cases} Z = A\sin\left(2\pi ft - \frac{\pi}{2}\right) + A \\ l = vt \end{cases} \quad (2)$$

where A is the vibration amplitude (μm), f is the vibration frequency (Hz), l is the distance traveled by the tool tip in the cutting direction (μm). v is the cutting speed (m/s), which can be expressed as:

$$v = \frac{n\pi R}{30} \quad (3)$$

Along with the ultrasonic vibration of the milling tool, the microstructures are generated during the rotary motion of the tool. Figure 3 shows the theoretical model of microstructures fabricated by AUVAM with no movement.

The microstructures fabricated with a commonly used milling tool (double edge) are illustrated in Fig. 3b. The microstructures are uniformly distributed around the axis, which are fan-shaped with a radius of approximately R and a maximum width of L at the circumference (Fig. 3c, d). Considering that R is normally much larger than L , L can be approximated as,

$$L = \frac{v}{f} \quad (4)$$

However, it is hardly to ensure that all microstructures are complete periodic structure units along the entire circumference. There are normally some incomplete microstructures as shown in red part in Fig. 3b. Therefore, the cutting

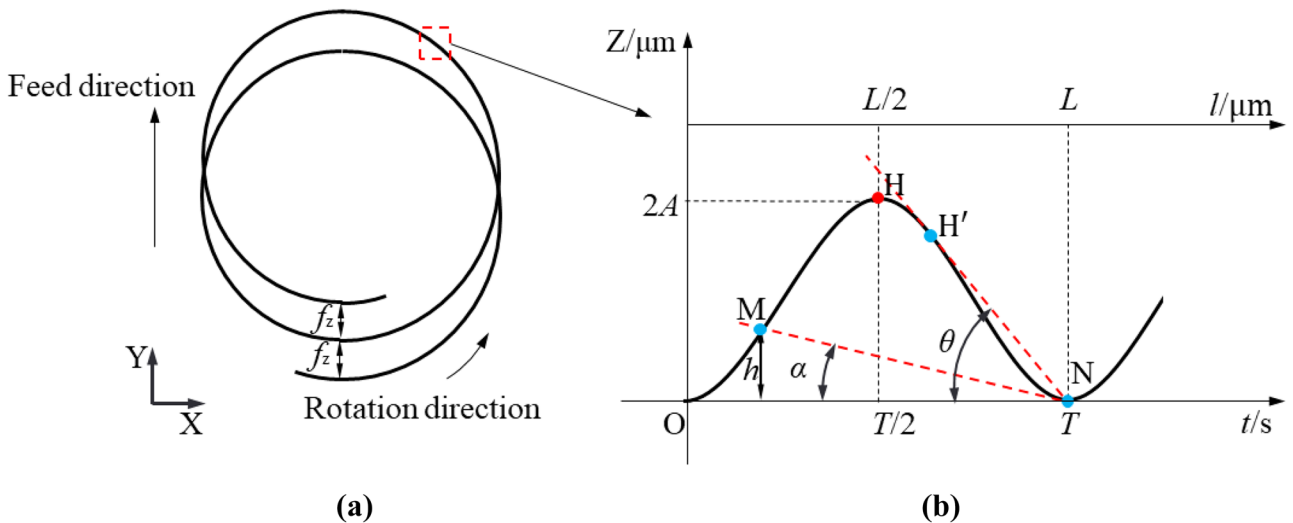


Fig. 2 Tool tip trajectory in AUVAM: **a** tool tip trajectory in X–Y plane; **b** tool tip trajectory in a vibration period

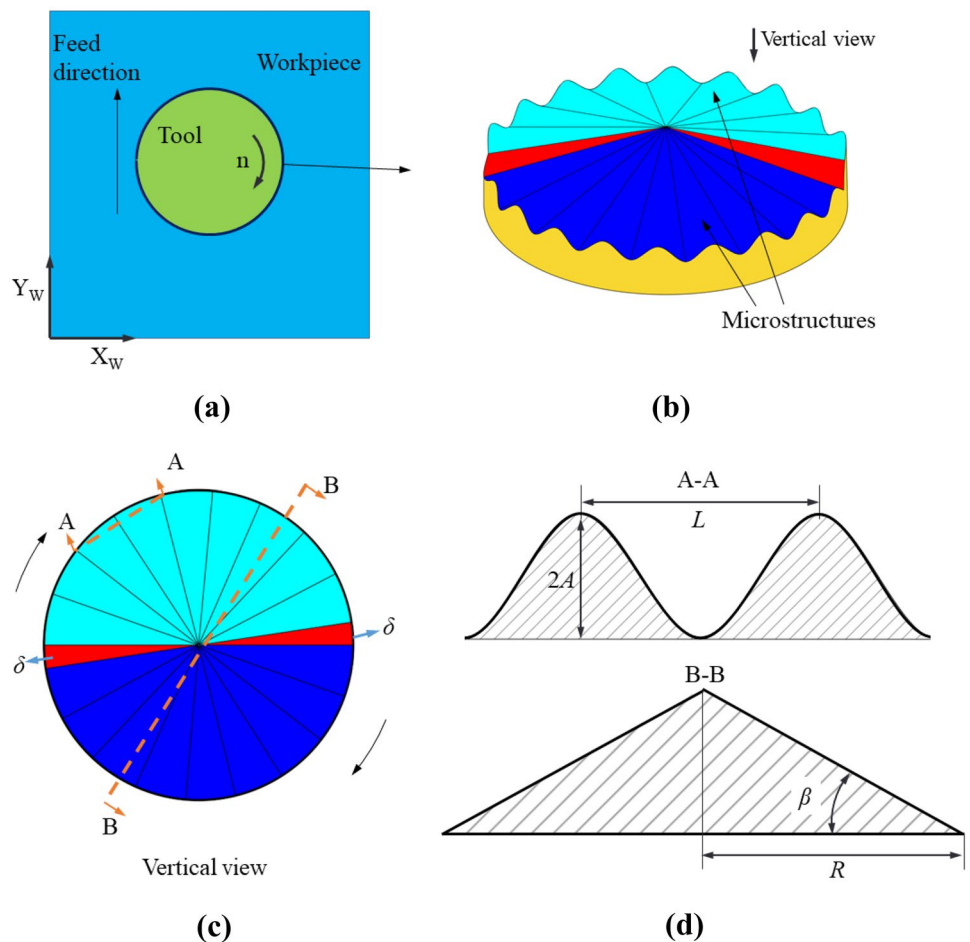
frequency ratio [35] proposed can describe the integrity of microstructures. The cutting frequency ratio of the half circle can be expressed as:

$$\lambda = \frac{30f}{n} = \Gamma + \varepsilon \tag{5}$$

where Γ is an integer part, ε is a decimal part. Γ determines the number of microstructures distributed on the circumference. The phase shift can be calculated by,

$$\delta = \frac{\pi\varepsilon}{\lambda} \tag{6}$$

Fig. 3 Theoretical model of microstructures fabricated by AUVAM: **a** schematic of processing; **b** arrangement and geometry of microstructures on surface; **c** vertical view; **d** sectional view



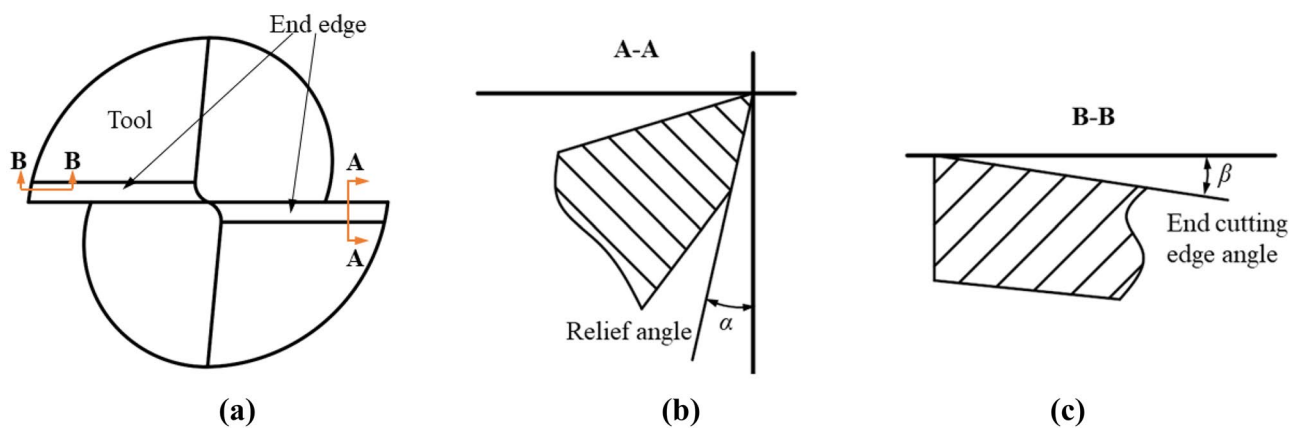


Fig. 4 Schematic diagram of tool angles: **a** vertical view of end edge; **b** sectional view of relief angle; **c** sectional view of end cutting edge angle

If $\epsilon > 0$, the phase difference δ exists, resulting in dislocation of the microstructures. If $\epsilon = 0$, there is no phase difference and periodic structure units are aligned in the feed direction.

In addition to the machining parameters, the tool angles also play an important role in the formation of the microstructures. The relief angle α and the end cutting edge angle β are the main tool angles of the tool end edge, and their schematic diagram is shown in Fig. 4.

The relief angle plays a significant role in the generation of the microstructures, as shown in Fig. 5. In the process of machining microstructures, the tool may overlap (blue area between points M and N) with the cutting trace to generate intersection point M when the tool moves from the highest point H of the trajectory to the lowest point N. The intersection angle between ON and MN theoretically equals to the relief angle α . Thus, the flank face squeezes the microstructure due to the overlap between them, resulting in the reducing of the microstructure height and the triangle-like shape (OMN).

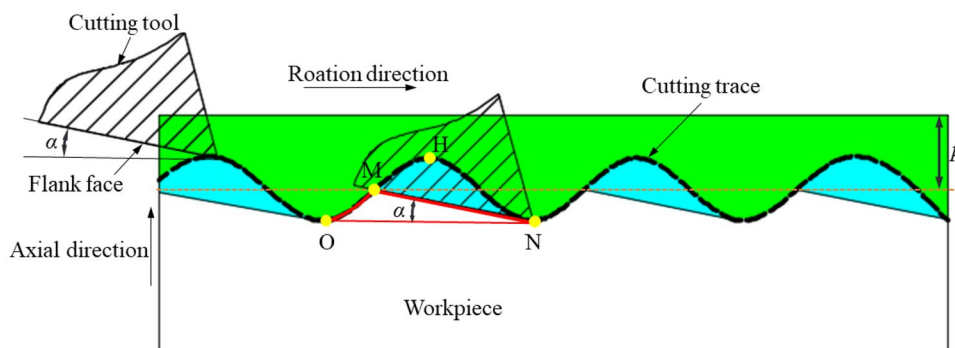
In order to further explore the role of the relief angle α in the generation of microstructures, as shown in Fig. 2b, the angle θ and value μ are defined [36],

$$\mu = \tan \theta = 1.37 \frac{120Af}{n\pi R} \tag{7}$$

If $\tan \alpha < \mu$, there is obvious overlap area between the flank face and the cutting trace, resulting in intersection point M as shown in Fig. 5. So the theoretical microstructure profile is triangle-like shown as OMN in Fig. 5. If $\tan \alpha \geq \mu$, there is no intersect between the flank face and profile of the microstructure. This result provides theoretical explanation for the difficulty of full reproduction of ultrasonic amplitude onto the height of the micro-texture in AUVAM [33, 34]. It also gives us valuable guidance of two possible ways for completely reproducing the ultrasonic amplitude (eliminating the overlap). The first way is directly increasing the angle α until $\tan \alpha \geq \mu$ by redesigning new milling tools. The second one is increasing the spindle speed n based on Eq. (7). The increase of the spindle speed makes μ decrease. So it is possible to fulfill $\tan \alpha \geq \mu$ when the spindle speed increases to a certain extent.

The above-mentioned process is only the formation of the microstructures during one rotation cycle of the milling tool. But in actual continuous machining process, just the edge part of the microstructures obtained in the last machining

Fig. 5 Illustration of the effect of relief angle on microstructures



cycle is retained, which can be divided into numerous identical micro-texture units. The rest part is covered by the microstructures which formed in the new rotation cycle, as shown in Fig. 6a. The length of the retained part is determined by the FPT. Consequently, the rotation of the tool continues to repeat the above process until the micro-texture units cover the entire workpiece surface, as shown in Fig. 6b. Figure 6b is an enlarged view of structures in the red dotted-line frame in Fig. 6a. It was validated by the observation of microstructures and micro-texture units resulting from experiment, as shown in Figs. S3 and S4.

Additionally, the end cutting edge angle β has little effect on the height and profile shape of the micro-texture units, but it causes height difference to generate 3D micro-texture units, as shown in Fig. 6c. The height difference Δh can be calculated by,

$$\Delta h = f_z \tan \beta \quad (8)$$

2.2 Simulation of micro-textured surface

The purpose of this part is to establish a mathematical simulation strategy of AUVAM based on the above theory. Firstly, a model was proposed to describe the geometrical characteristics of the tool. Thereafter, both the rotation and feed motion of the tool were considered to calculate the trajectory of the cutter. Based on the trajectory, the generation process of the micro-texture was presented by Z-map algorithm model.

2.2.1 The tool model

The end edge of the milling tool is mainly composed of the rake face, flank face and the blade at the intersection of the two faces [37]. Tao et al. [38] and Gao et al. [39]

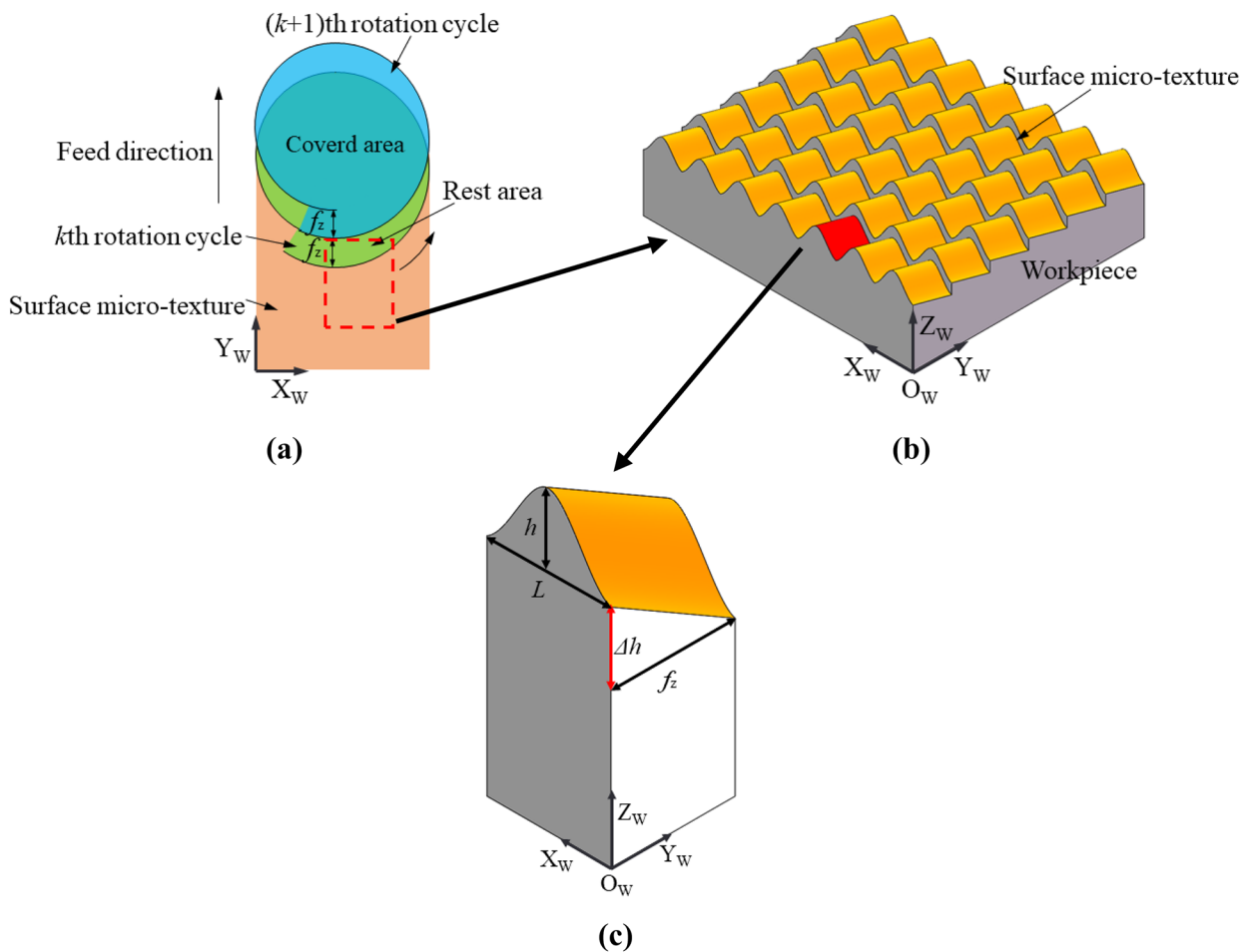


Fig. 6 Schematic diagram of micro-texture surface by AUVAM: **a** fabrication of micro-texture units; **b** micro-textured surface; **c** micro-texture unit

simplified the double-edge end milling tool as a 2D profile line of the blade edge, which was composed of two symmetrical straight lines. However, the 2D line model is not competent to describe the detailed effect of milling tool due to the absence of the flank face, which is vital to the generation of the micro-texture as analyzed in Sect. 2.1. Therefore, a 3D tool model considering the flank face is proposed, as shown in Fig. 7.

To simplify the above model, several assumptions are made as follows: i) the blade edge has a radius R_B , which decreases with the increase of the relief angle according to the measurement of experiment; ii) only the flank face and blade are in contact with the workpiece (ignoring the effect of rake face), which are smooth, continuous and symmetrical; iii) the plastic deformation of the material is not considered. The 3D tool (flank face and blade) can be fully described by a set of parametric functions:

$$\begin{cases} x = (-1)^{(p+1)}x & 0 < x < R \\ y = (-1)^{(p+1)}y & 0 < y < D \\ z = \frac{\sqrt{(R_B^2 - (y - R_B)^2)(R^2 + (R \tan \beta)^2) - x R \tan \beta}}{-(x - R) \tan \alpha + (y - R_B \tan \beta + R_B) \tan \beta + R_B(1 - \cos \alpha)} + R_B \tan \beta + R_B & 0 < y < (1 + \sin \alpha)R_B \\ & (1 + \sin \alpha)R_B < y < D \end{cases} \quad (9)$$

where D is the width of flank face, $p = 1, 2$, is the number of the tool blade.

2.2.2 Simulation of the micro-textured surface

Simulation of the formation process for micro-texture has become a useful method to explore the machining mechanism and predict surface topography. Kilic and Altintas [37] used homogeneous transformation matrices to realize the simulation of machining operations. Zhu et al. [40] presented the visualization of UVAM to show the intermittent cutting process. Gao et al. [39] obtained the surface topography machined by milling based on the Z-map

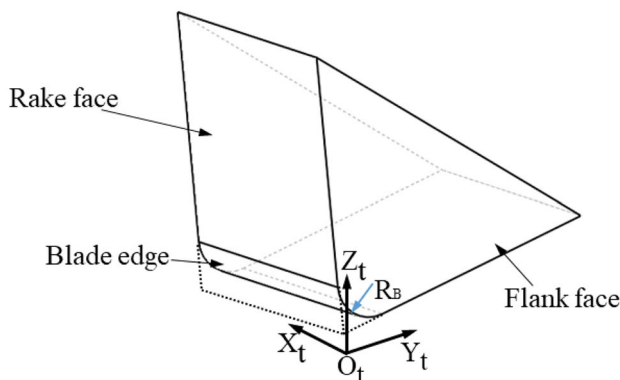


Fig. 7 Blade edge geometry definition

algorithm, and the simulation results were in good agreement with the experimental results. Liu et al. [36] took the geometry of the tool into account when establishing simulation model of the surface in ultrasonic vibration-assisted turning. Although there are some in-depth studies on the simulation of other machining process, research on the simulation of AUVAM is scarce until now. Consequently, we proposed a simulation strategy for AUVAM and developed the corresponding numerical calculation program in MATLAB based on the aforementioned theoretical model and simulation methods.

As shown in Fig. 8, $O_t-X_tY_tZ_t$ is set at tool local coordinate system, in which the parametric functions describing the tool model are employed. The tool local coordinate system rotates with the tool. $O_T-X_TY_TZ_T$ is set at tool coordinate system, which translates and vibrates with the tool. The O_T and Z_T coincide with O_t and Z_t , respectively.

$O_w-X_wY_wZ_w$ is set at the workpiece coordinate system, which is fixed with the workpiece, Y_w is the feed direction, X_w is the radial direction, and Z_w is the axial direction.

In the tool local coordinate system, kinematic equation of tool model in Sect. 2.2.1 can be written as follows:

$$\begin{bmatrix} x_t \\ y_t \\ z_t \\ 1 \end{bmatrix} = \begin{bmatrix} x \\ y \\ z \\ 1 \end{bmatrix} \quad (10)$$

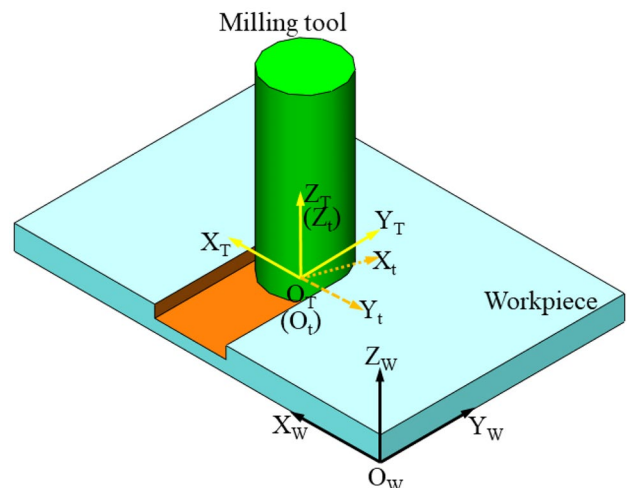


Fig. 8 Space coordinate systems for AUVAM

Equation (10) can be transferred to the workpiece coordinate system by homogeneous matrix transformation method [37]. There is a rotation angle k from the tool local coordinate system to the tool coordinate system, and the transformation matrix of any point from the tool local coordinate system to the tool coordinate system can be expressed as:

$$T_T = \begin{bmatrix} \cos k & \sin k & 0 & 0 \\ -\sin k & \cos k & 0 & 0 \\ 0 & 0 & 1 & 0 \\ 0 & 0 & 0 & 1 \end{bmatrix} \quad (11)$$

There is only a relative translation relation between tool coordinate system and workpiece coordinate system. The position of the tool coordinate system in the workpiece coordinate system can be derived as follows:

$$\begin{cases} x_T = x_0 \\ y_T = y_0 + V_f t \\ z_T = z_0 + A \sin(2\pi f t) \end{cases} \quad (12)$$

where (x_0, y_0, z_0) is the position of the origin at the tool coordinate system relative to the origin at the workpiece coordinate system, V_f is the feed speed along Y-axis, t is the running time, A is the ultrasonic amplitude, f is the ultrasonic vibration frequency. Then, the transformation matrix of any point from the tool coordinate system to the workpiece coordinate system can be derived as follows:

$$T_w = \begin{bmatrix} 1 & 0 & 0 & x_0 \\ 0 & 1 & 0 & y_0 + V_f t \\ 0 & 0 & 1 & z_0 + A \sin(2\pi f t) \\ 0 & 0 & 0 & 1 \end{bmatrix} \quad (13)$$

By combining Eqs. (9)–(13), trajectory equation of any point of the tool in the workpiece coordinate system can be obtained as follows:

$$\begin{bmatrix} x_w \\ y_w \\ z_w \\ 1 \end{bmatrix} = T_w T_T \begin{bmatrix} x_t \\ y_t \\ z_t \\ 1 \end{bmatrix} = \begin{bmatrix} x \cos k - y \sin k + x_0 \\ x \sin k - y \cos k + y_0 + V_f t \\ z + z_0 + A \sin(2\pi f t) \\ 1 \end{bmatrix} \quad (14)$$

Based on the Z-map algorithm model [39], the mathematical model of the AUVAM is established with the trajectory equation. The workpiece and the tool model are discretized into a series of points for numerical calculation. The trajectory swept is converted into a discrete point cloud of $[z_w]$ value, which is one-to-one matched with the grid points on the workpiece surface. The $[z_w]$ value of discrete cloud points replaces the height $[Z_w]$ of the points on the workpiece to generate the surface topography once the $[z_w]$ is smaller than the $[Z_w]$.

3 Experimental details

The experiment of AUVAM was carried out on a CNC milling machine, as shown in Fig. 9. The ultrasonic system was mainly composed of three parts: the power controller, the ultrasonic transducer and the horn. The power controller converted ordinary electrical signals into ultrasonic electrical signals with frequency of 21 kHz. The ultrasonic transducer converted electrical signal into ultrasonic mechanical vibration by piezo ceramic plates. The horn further amplified the generated ultrasonic vibration with amplitude of 2 μm , which was transmitted to the milling tool installed on the horn. The employed tool was a cemented carbide end milling with a diameter of 2 mm, as shown in Fig. 10.

The sample material was aluminum alloy 7075, and the sample size was 20 \times 20 \times 4 mm. Besides the conventional milling tool with relief angle of 10°, some special tools with relief angles of 20°, 30°, and 40° were customized for the experiments. In order to ensure material was removed continuously during experiment, the cutting depth of milling tool was set as a constant value of 10 μm , which was much higher than ultrasonic amplitude. The detailed experimental parameters are shown in Table 1, and each experiment was repeated 5 times. After milling, all the samples were ultrasonically cleaned with anhydrous ethanol twice and then blow-dried by the air compressor. The surface morphologies after milling were observed and measured by a hyperfocal 3D microscope (VHX-7000).

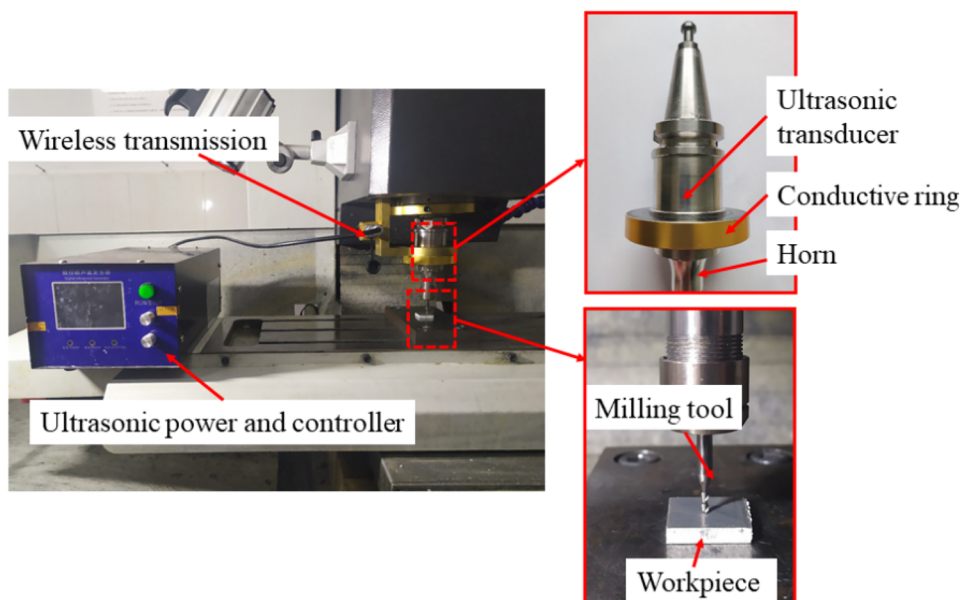
4 Results and discussion

4.1 Effect of relief angle on micro-texture

Figure 11 shows the profile of micro-textured results from experiment and simulation with different relief angles (ranged from 10° to 40°) under the spindle speed of 2000 rpm and ultrasonic amplitude of 2 μm . Micro-texture with height of 0.8 μm and width of 10 μm was obtained under the relief angle of 40°. It was illustrated that the height of the profile increased with the increase of the relief angle in both experimental and simulation results, which suggested that the relief angle significantly affected the texture height, as shown in Fig. 11. This influence was mainly caused by the overlap between the flank surface of the tool and the profile of the micro-texture, as shown in Fig. 12. The overlapped area decreased with the increase of relief angle resulting in the rise of the texture height. Consequently, there should be no overlapped area when the relief angle was large enough, as shown in Fig. 12d.

However, the height of the micro-texture in simulation was apparently larger than that in experiment. The reason

Fig. 9 Experimental setup for AUVAM



was that the plastic deformation caused by the tool extrusion was not considered in simulation. As the width of the micro-texture was only 10 μm and decreased with the rise of height, the micro-texture was easily deformed under the extrusion force from the flank face. Besides, all the profiles were smoothly sinusoid-like curves in experiment but those were triangular curves in simulation. The difference between the profile shape in experiment and simulation also confirmed the obvious influence of the plastic deformation caused by extrusion with the spindle speed of 2000 rpm.

The peak offset $((l_1 - L/2)/L)$ of the micro-textured profile existed in both experimental and simulation results, as shown in Fig. 11a, b, d. And the peak of each micro-textured profile unit noticeably shifted to the right with the increase of the relief angle. The peak offset in experimental results

could reach more than 10% of the micro-textured width with the relief angle of 10°. And it was negligible under the relief angle of 40°. Interestingly, the peak offset of simulation was smaller than that of experiment correspondingly due to the ignorance of plastic deformation in simulation. This difference further confirmed the existence of extrusion, which was also caused by the overlap between the flank surface and the micro-textured profile, as shown in Fig. 12.

4.2 Effect of spindle speed on micro-texture

Figure 13 shows the experimental and simulation results of micro-textured profiles under different spindle speeds (ranged from 2000 to 8000 rpm with interval of 2000 rpm) with the relief angle of 10°. It was indicated that the height of the texture obviously increased with the rise of the spindle speed in both experiment and simulation. It suggested that the spindle speed of the milling tool significantly affected the textured height. Nevertheless, the heights in simulation

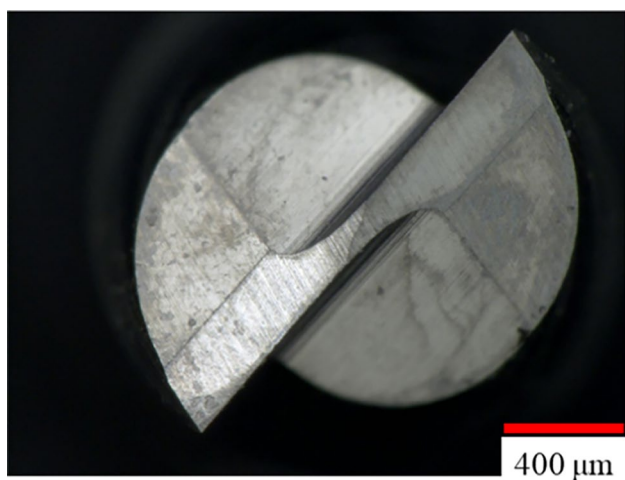


Fig. 10 Micrograph of milling tool

Table 1 Experimental parameters

| | | |
|----------------------|---------------------------|--|
| Workpiece | Material | Al7075 |
| Tool geometry | Relief angle (°) | 10, 20, 30, 40 |
| | End cutting edge angle(°) | 1.5 |
| Vibration conditions | Frequency(kHz) | 21 |
| | Amplitude(um) | 2 |
| Cutting conditions | Spindle speed (rpm) | 2000, 3000, 4000, 5000, 6000, 7000, 8000 |
| | Feed per tooth (μm) | 10, 50, 100, 150 |
| | Depth of cut (μm) | 10 |
| | | |

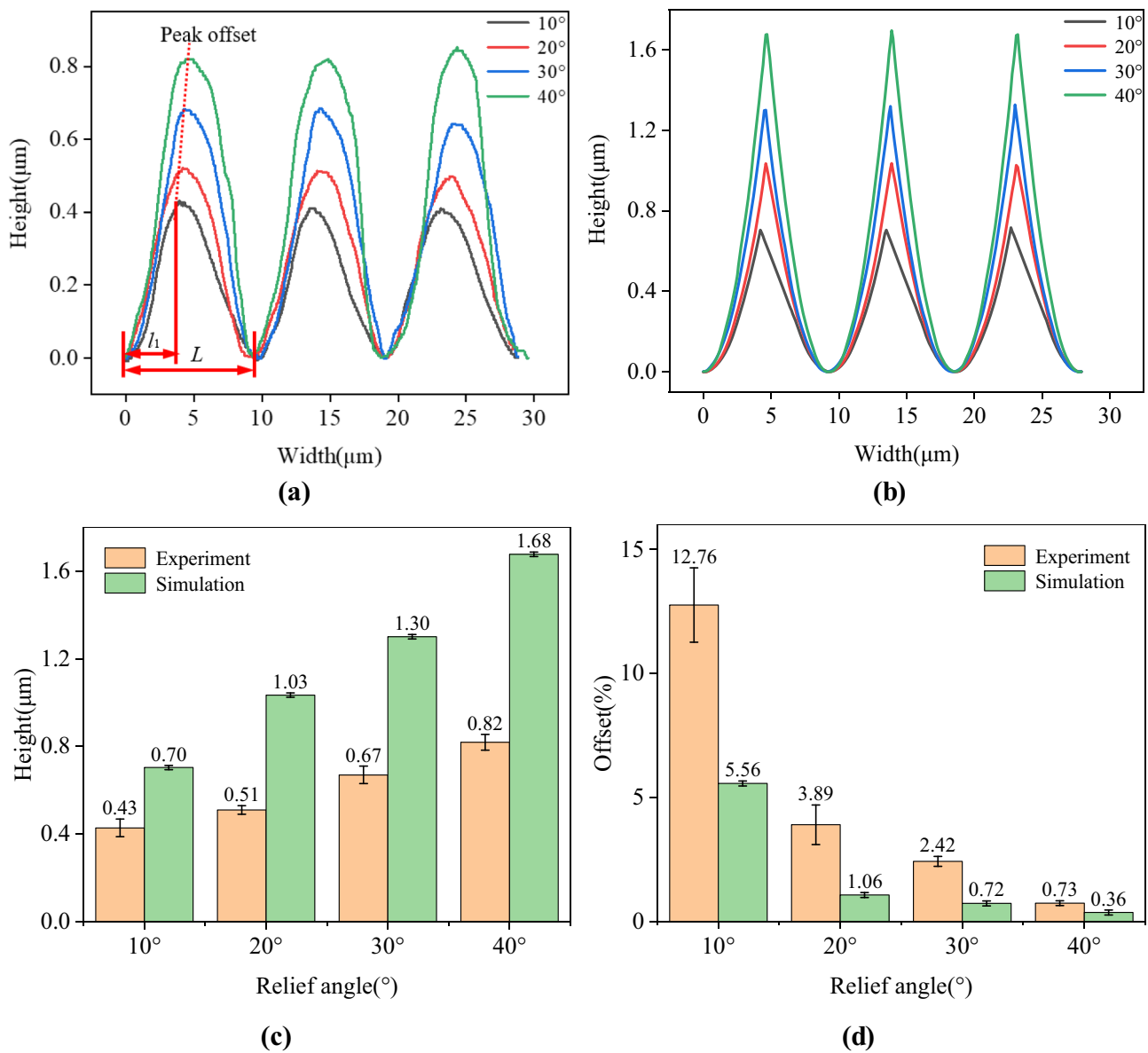


Fig. 11 Experimental and simulation results with relief angles ranged from 10° to 40° ($n=2000$ rpm): **a** experimental micro-textured profile; **b** simulation micro-textured profile; **c** height of micro-textured profile; **d** peak offset of micro-textured profile

were obviously higher than those in experiment under low spindle speed, but the heights in both simulation and experiment tended to be consistent as the increase of spindle speed. Moreover, all the profiles were sinusoid-like curves

in experiment, but the profiles gradually changed from triangular to sinusoid-like curves in simulation.

The above results implied that both the micro-textured height and profile in simulation and experiment became

Fig. 12 Schematic diagram of overlap as the relief angle increases

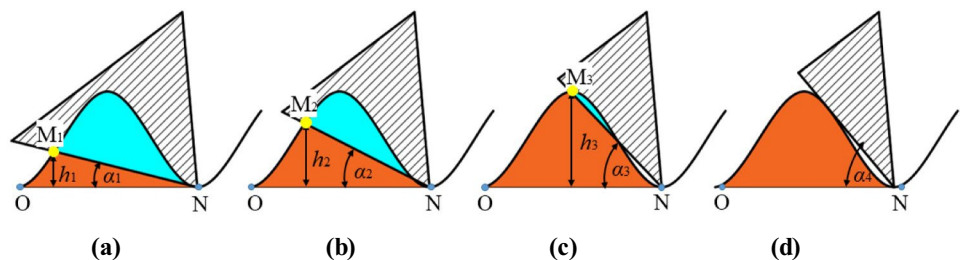
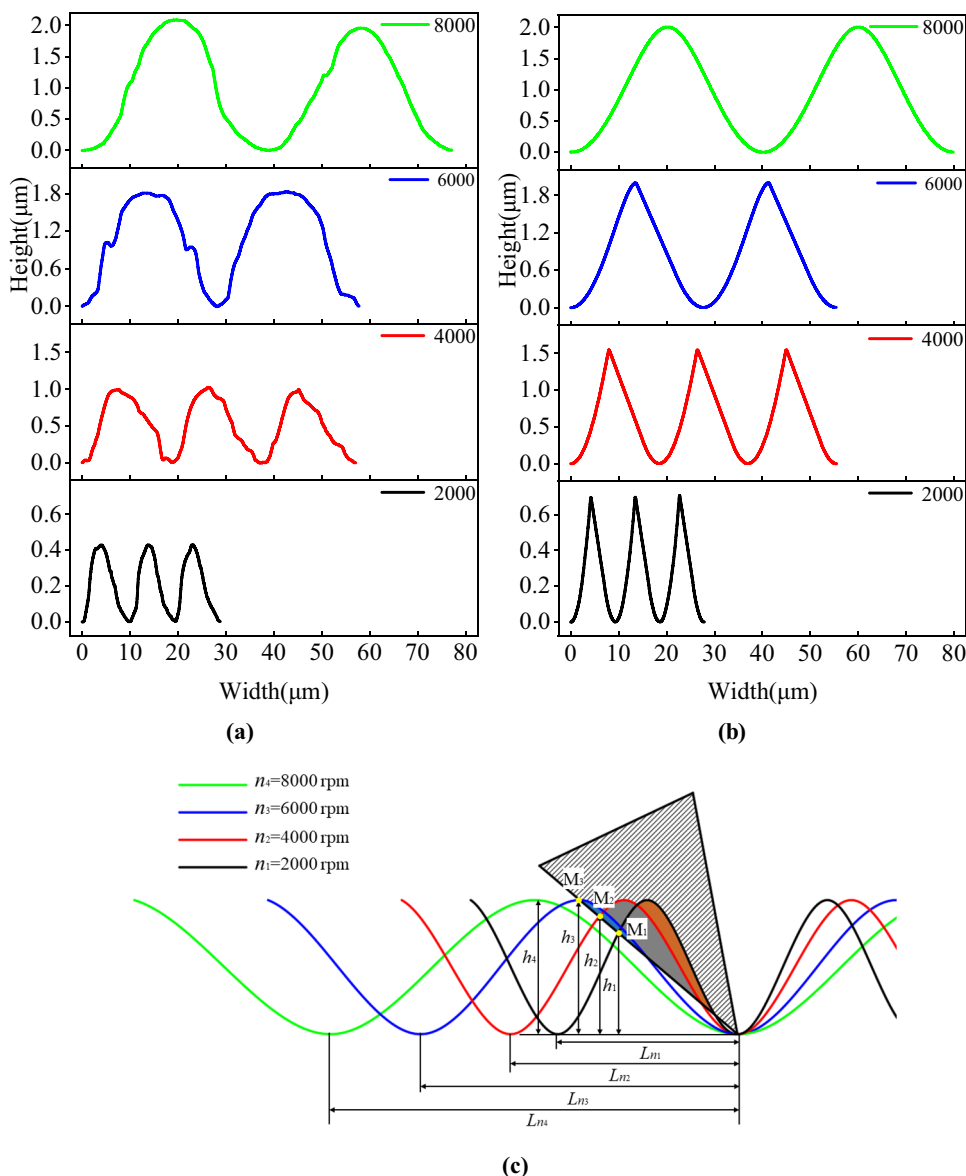


Fig. 13 Experimental and simulation results with spindle speeds ranged from 2000 to 8000 rpm (relief angle of 10°): **a** experimental micro-textured profile; **b** simulation micro-textured profile; **c** schematic diagram of overlap as spindle speed increases



more consistent with the increase of spindle speed. It could be explained mainly from the following two aspects:

- (i) The overlapped area between the flank surface of the cutter and the micro-textured profile decreased with the increase of spindle speed, as shown in Fig. 13c. Therefore, the influence of the overlap on the height and profile diminished. Furthermore, there was completely no overlapped area when the spindle speed was 8000 rpm.
- (ii) With the comparison among L_{n1}, L_{n2}, L_{n3} and L_{n4} in Fig. 13c, it was easy to conclude that the width of the micro-texture unit dramatically increased with the rise of spindle speed, resulting from larger traveled distance of the cutter in a vibration period. Consequently, the increase of width greatly enhanced the deformation resistance of the micro-texture unit. Hence, the effects

of the extrusion on the generation of micro-texture decreased as the spindle speed increased.

Figure 14 shows more detailed experimental results of height and peak offset with spindle speeds ranged from 2000 to 8000 rpm with interval of 1000 rpm. The difference of both micro-textured height and peak offset between simulation and experimental results gradually decreased with the increase of the spindle speed. The micro-textured heights in experiment were almost the same with those in simulation under the spindle speed above 7000 rpm, as shown in Fig. 14a. And there was no obvious peak offset of the micro-textured profile with the spindle speed above 7000 rpm, as shown in Fig. 14b. The detailed profile of micro-texture can be found in Fig. S1. The above results indicated that the influences of the overlap and extrusion between the milling tool and the micro-textured profile

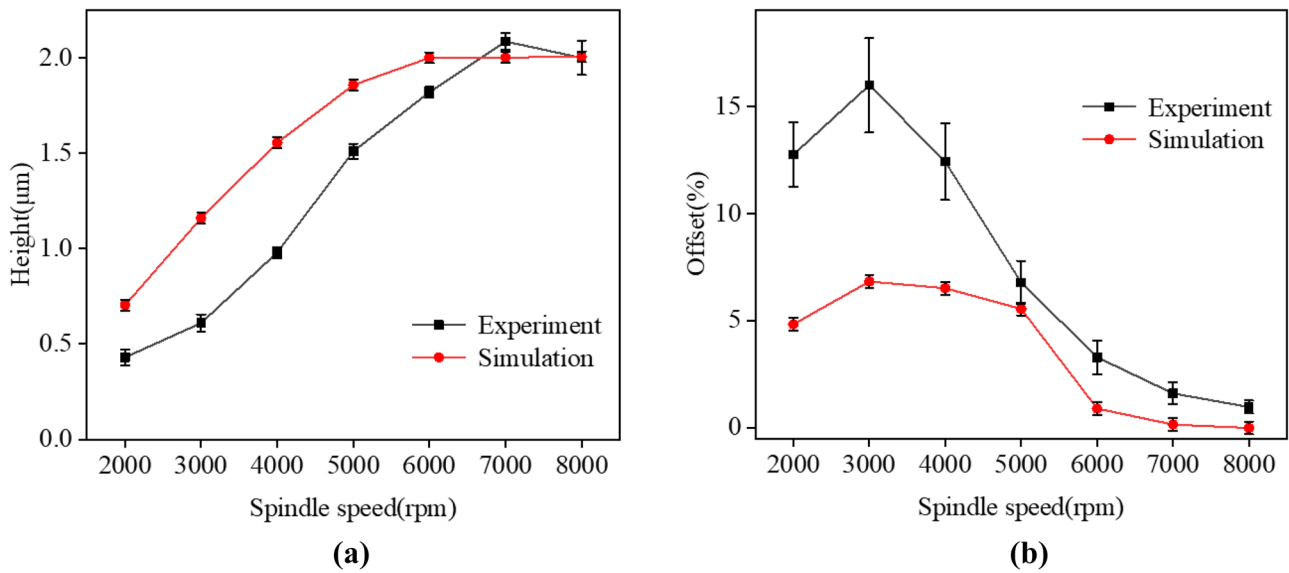


Fig. 14 Experimental and simulation results with spindle speeds ranged from 2000 to 8000 rpm (relief angle of 10°): **a** height of micro-textured profile; **b** peak offset of micro-textured profile

were negligible when the spindle speed was large enough. Specifically, smooth sinusoid-shaped micro-texture with minimum width of 35 μm (determined by the spindle speed of 7000 rpm) and height of 2 μm (the same as the ultrasonic amplitude) was achieved under the relief angle of 10°.

Generally, under the combined effect of the reduction of overlap and the increase of the micro-texture unit width, the height of micro-texture obviously increased and the profile was closer to the theoretical sinusoid with the rise of the spindle speed. It was worthy to notice that the ultrasonic amplitude could be fully reproduced onto the height of the micro-texture with large

enough spindle speed even using an ordinary milling tool (with relief angle of 10°). However, the width of this type of micro-texture unit was normally too large for most applications of micro-texture.

4.3 Coupling effect of relief angle and spindle speed on micro-texture

Figure 15 shows the heights of the micro-texture with different relief angles under various spindle speeds.

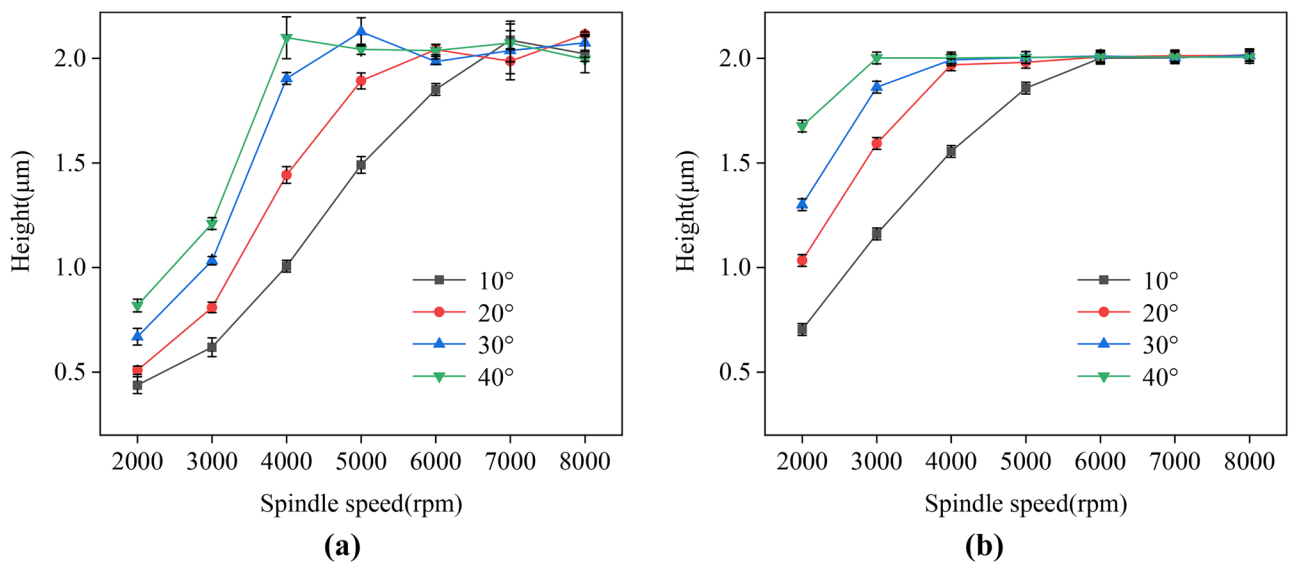
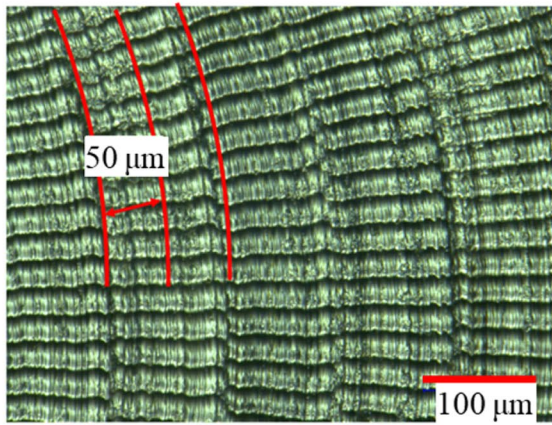
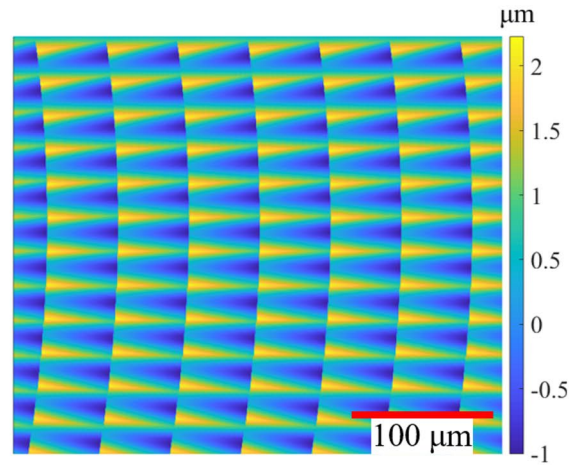


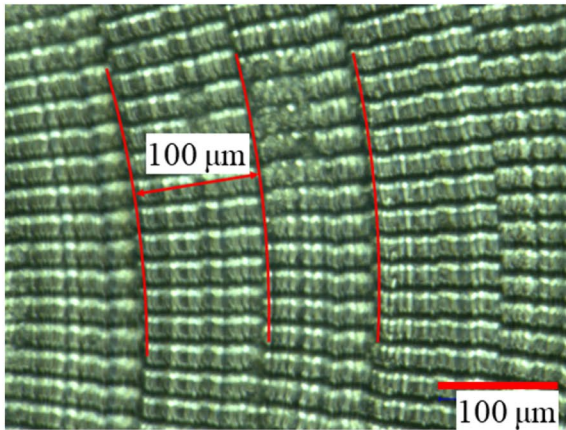
Fig. 15 Height of the micro-texture with different relief angles under various spindle speeds: **a** experimental results; **b** simulation results



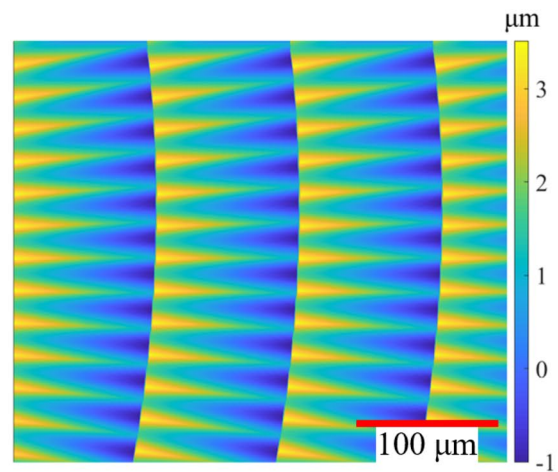
(a) FPT=50 μm



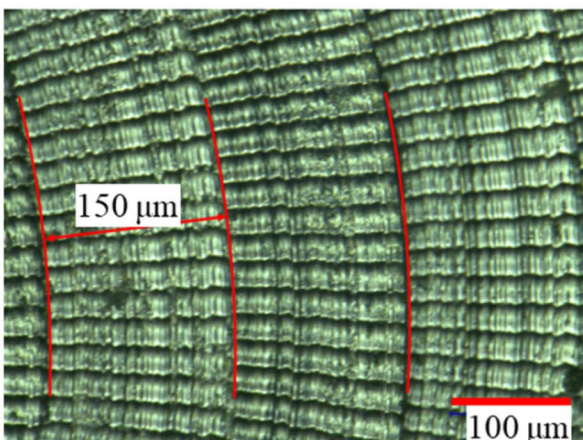
(b) FPT =50 μm



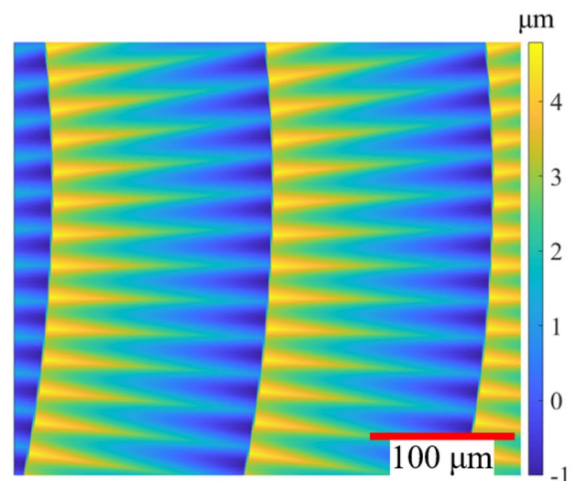
(c) FPT =100 μm



(d) FPT =100 μm



(e) FPT =150 μm



(f) FPT =150 μm

Fig. 16 Results of micro-textured surface at different FPTs ($n = 5000$ rpm, $\alpha = 10^\circ$): **a, c, e** experimental results; **b, d, f** simulation results

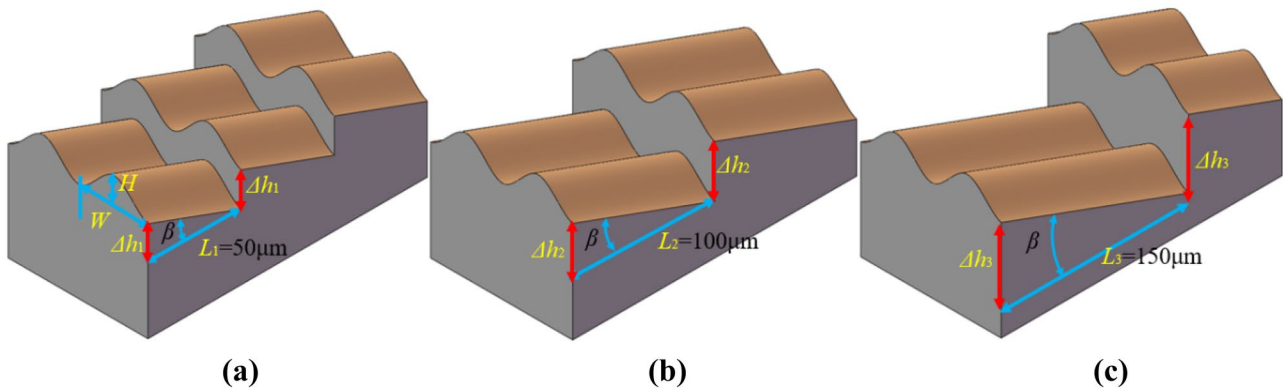
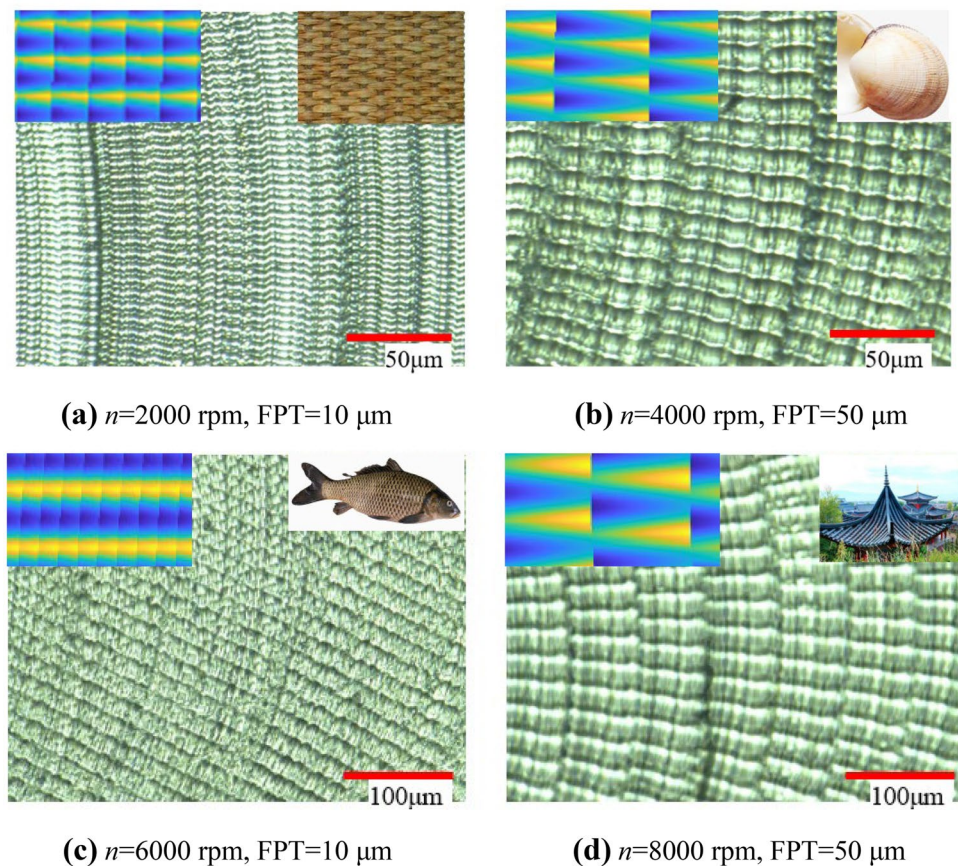


Fig. 17 The schematic diagram of the micro-texture units at different FPTs: **a** FPT = 50 μm ; **b** FPT = 100 μm ; **c** FPT = 150 μm

Both the experimental and simulation results illustrated that the micro-textured height rose to 2 μm (the ultrasonic amplitude) then remained almost constant with the increase of spindle speed for all relief angles. The detailed profile of micro-texture is shown in Fig. S2. The above results suggested that the maximum textured height depended on the ultrasonic amplitude in AUVAM. Whereas the minimum spindle speed for the maximum height of micro-texture was different with various relief angles. Here we used MSS to present the minimum

spindle speed to fully reproduce the ultrasonic amplitude onto the height of micro-texture. The MSSs for the relief angle of 10°, 20°, 30°, and 40° were 7000, 6000, 5000, and 4000 rpm in experimental results, which implied that the MSSs decreased with the increase of relief angle. The simulation results confirmed that the MSSs decreased with the rise of relief angle. But the simulation MSSs were a little lower than the corresponding value from experiment due to the ignorance of plastic deformation in numerical calculation.

Fig. 18 Typical textures at different processing parameters in AUVAM: **a** weave texture; **b** shell texture; **c** fish scale texture; **d** corrugated texture



The increase of both relief angle and spindle speed resulted in the decrease of the overlap area between the flank surface and the micro-textured profile, as analyzed in Sects. 4.1 and 4.2. Therefore, larger relief angle could decrease the MSS leading to full-height micro-texture with smaller width. Moreover, smooth sinusoid-shaped micro-texture with minimum width of 20 μm and height of 2 μm (the same as the ultrasonic amplitude) was realized under the relief angle of 40°. The feature size was significantly reduced by almost a half compared with that obtained by the ordinary tool (the relief angle of 10°). It was concluded that the profile (including height, width and the shape) of the micro-texture unit could be effectively regulated by relief angle and spindle speed.

4.4 Regulation of micro-textured surface

Besides the height, width and profile shape, another important parameter for characterizing the micro-texture unit is the length of the unit, which is dominated by FPT during the milling process. Figure 16 shows the experimental and simulation results of the micro-textured surface under different FPTs of 50, 100 and 150 μm with the relief angle of 10° and spindle speed of 5000 rpm. It was illustrated that all the lengths of the micro-texture unit coincided well with the corresponding FPTs both in experimental and simulation results. The schematic diagram of the micro-texture unit is shown in Fig. 17. It was demonstrated that the micro-texture unit was inclined 3D morphology, and the inclination angle β was determined by the end cutting edge angle of the milling tool. Therefore, there was a height difference Δh between two adjacent groups of the micro-texture units in the length direction. Not only the unit length but also the height difference increased with the increase of FPT. Consequently, complex 3D micro-texture units with controllable height difference could be fabricated onto the entire surface of the workpiece by AUVAM.

We further fabricated four typical textures of weave, shell, fish scale, and corrugation even using ordinary milling tool (relief angle of 10°) through selecting different processing parameters, as shown in Fig. 18a–d. Based on the above analysis, the surface texture was formed by arranging the micro-texture units in accordance with the tool trajectory. The length and width of the micro-texture unit can be adjusted through FPT and spindle speed. The height of the micro-texture unit can be further adjusted by the relief angle of milling tool as discussed in Sect. 4.1. Therefore, it is possible to regulate the arrangement, morphology and height of the micro-texture unit by changing the processing parameters and milling tool, resulting in desirable complex 3D micro-textured surface.

5 Conclusions

In this study, the generation mechanism and major influence factors of the micro-texture fabricated by AUVAM were explored through simulation and experiment. The simulation results agreed well with that of experiment, which provided an effective prediction method for surface topography during AUVAM.

Based on the results and analysis, the following conclusions can be drawn:

- (i) Cutting and squeezing from the flank surface of milling tool were the main generation mechanism of micro-texture in AUVAM.
- (ii) The height of micro-textured profile was significantly increased and the shape of micro-textured profile changed from triangular to sinusoid-like with the increase of relief angle and spindle speed.
- (iii) With the coupling influence of the relief angle and spindle speed, sinusoid-shaped micro-texture with minimum width of 20 μm and height of 2 μm (the same as the ultrasonic amplitude) was realized under the relief angle of 40° and MSS of 4000 rpm.

Moreover, the fabricated typical textures illustrated that the arrangement, morphology and height of the micro-texture unit could be effectively regulated by changing the processing parameters and milling tool to obtain desirable complex 3D micro-textured surface. This study not only clarified the mechanism of AUVAM, but also provided a potential mass-production method for fabrication of micro-texture.

Supplementary Information The online version contains supplementary material available at <https://doi.org/10.1007/s00170-022-09974-8>.

Acknowledgements The authors sincerely appreciate financial supports from Fundamental Research Funds for the Central Universities (19CX02020A) and the National Natural Science Foundation of China (51905546), Key Technology Research and Development Program of Shandong (2018GGX103034).

Author contribution First author contributions established theoretical model, conceived and designed experiments, analyzed the data and wrote the initial manuscript. Corresponding author contributions received editor correspondence and send in revisions. Second author contributions established theoretical model, performed the experiments; analyzed the data; contributed on the writing of the manuscript. Other co-authors contributions: all co-authors have almost contributed equally. The major work involved is as follows: performed the experiments; contributed to reagents and materials; sent the sample to the test; analyzed the data; and reviewed each paper draft.

Declarations

Competing Interests The authors declare that they have no known competing financial interests or personal relationships that could have appeared to influence the work reported in this paper.

References

- Jiang Y, Shen H, Pu T, Zheng C, Tang Q, Gao K, Wu J, Rui C, Li Y, Liu Y (2017) High efficiency multi-crystalline silicon solar cell with inverted pyramid nanostructure. *Sol Energy* 142:91–96. <https://doi.org/10.1016/j.solener.2016.12.007>
- Li L, Yi AY (2010) Development of a 3D artificial compound eye. *Opt Express* 18:18125–18137. <https://doi.org/10.1364/oe.18.018125>
- Sun J, Luo X, Chang W, Ritchie JM, Chien J, Lee A (2012) Fabrication of periodic nanostructures by single-point diamond turning with focused ion beam built tool tips. *J Micromech Microeng.* <https://doi.org/10.1088/0960-1317/22/11/115014>
- Jahed Z, Molladavoodi S, Seo BB, Gorbet M, Tsui TY, Mofrad MR (2014) Cell responses to metallic nanostructure arrays with complex geometries. *Biomaterials* 35:9363–9371. <https://doi.org/10.1016/j.biomaterials.2014.07.022>
- Jeon H, Simon CG JR, Kim G (2014) A mini-review: Cell response to microscale, nanoscale, and hierarchical patterning of surface structure. *J Biomed Mater Res B Appl Biomater* 102:1580–1594 <https://doi.org/10.1002/jbm.b.33158>
- Zhang J, Tian W, Chen J, Yu J, Zhang J, Chen J (2019) The application of polyetheretherketone (PEEK) implants in cranioplasty. *Brain Res Bull* 153:143–149. <https://doi.org/10.1016/j.brainresbull.2019.08.010>
- Zhao W, Wang L, Xue Q (2010) Design and fabrication of nanopillar patterned textures for improving nanotribological performance. *ACS Appl Mater Interfaces* 2:788–794. <https://doi.org/10.1021/am900788t>
- Zhang S, Zhou Y, Zhang H, Xiong Z, To S (2019) Advances in ultra-precision machining of micro-structured functional surfaces and their typical applications. *Int J Mach Tools Manuf* 142:16–41. <https://doi.org/10.1016/j.ijmactools.2019.04.009>
- Hosseinabadi HN, Sajjadi SA, Amini S (2018) Creating micro textured surfaces for the improvement of surface wettability through ultrasonic vibration assisted turning. *Int J Adv Manuf Technol* 96:2825–2839. <https://doi.org/10.1007/s00170-018-1580-2>
- Chowdhury H, Loganathan B, Wang Y, Mustary I, Alam F (2016) A Study of Dimple Characteristics on Golf Ball Drag. *Procedia Eng* 147:87–91. <https://doi.org/10.1016/j.proeng.2016.06.194>
- Chen X, Zhai W, Dong S, Zheng K, Xu R, Wang J, Liu X, Lu W (2020) Investigations on torsional fretting wear properties of CuAlNi processed by ultrasonic vibration-assisted milling. *Tribol Int.* <https://doi.org/10.1016/j.triboint.2020.106238>
- Hussain SQ, Ahn S, Park H, Kwon G, Raja J, Lee Y, Balaji N, Kim H, Le AHT, Yi J (2013) Light trapping scheme of ICP-RIE glass texturing by SF₆/Ar plasma for high haze ratio. *Vacuum* 94:87–91. <https://doi.org/10.1016/j.vacuum.2013.01.026>
- Liu X, Li Y (2011) Analysis of LIGA-Ni Microstructure. *AEMT, Sanya, PEOPLES R CHINA* 284–286:1574–1578. <https://doi.org/10.4028/www.scientific.net/AMR.284-286.1574>
- Borjali A, Monson K, Raeymaekers B (2018) Friction between a polyethylene pin and a microtextured CoCrMo disc, and its correlation to polyethylene wear, as a function of sliding velocity and contact pressure, in the context of metal-on-polyethylene prosthetic hip implants. *Tribol Int* 127:568–574. <https://doi.org/10.1016/j.triboint.2018.07.005>
- Koyano T, Hosokawa A, Takahashi T, Ueda T (2019) One-process surface texturing of a large area by electrochemical machining with short voltage pulses. *CIRP Ann* 68:181–184. <https://doi.org/10.1016/j.cirp.2019.04.100>
- Xu S, Kuriyagawa T, Shimada K, Mizutani M (2017) Recent advances in ultrasonic-assisted machining for the fabrication of micro/nano-textured surfaces. *Front Mech Eng China* 12:33–45. <https://doi.org/10.1007/s11465-017-0422-5>
- Liu Q, Xu J, Yu H (2020) Experimental study of tool wear and its effects on cutting process of ultrasonic-assisted milling of Ti6Al4V. *Int J Adv Manuf Technol* 108:2917–2928. <https://doi.org/10.1007/s00170-020-05593-3>
- Verma GC, Pandey PM, Dixit US (2018) Modeling of static machining force in axial ultrasonic-vibration assisted milling considering acoustic softening. *Int J Mech Sci* 136:1–16. <https://doi.org/10.1016/j.ijmecsci.2017.11.048>
- Ni C, Zhu L (2020) Investigation on machining characteristics of TC4 alloy by simultaneous application of ultrasonic vibration assisted milling (UVAM) and economical-environmental MQL technology. *J Mater Process Technol.* <https://doi.org/10.1016/j.jmatprotec.2019.116518>
- Chen G, Ren C, Zou Y, Qin X, Lu L, Li S (2019) Mechanism for material removal in ultrasonic vibration helical milling of Ti 6Al 4V alloy. *Int J Mach Tools Manuf* 138:1–13. <https://doi.org/10.1016/j.ijmactools.2018.11.001>
- Baraheni M, Amini S (2020) Mathematical model to predict cutting force in rotary ultrasonic assisted end grinding of Si₃N₄ considering both ductile and brittle deformation. *Measurement.* <https://doi.org/10.1016/j.measurement.2020.107586>
- Amini S, Baraheni M, Khaki M (2021) Empirical study on ultrasonic assisted turn-milling. *Proc. Inst. Mech. Eng. Part E: J Process Mech Eng* 235:1469–1478. <https://doi.org/10.1177/09544089211008714>
- Feng Y, Hsu FC, Lu YT, Lin YF, Lin CT, Lin CF, Lu YC, Liang SY (2019) Residual stress prediction in ultrasonic vibration-assisted milling. *Int J Adv Manuf Technol* 104:2579–2592. <https://doi.org/10.1007/s00170-019-04109-y>
- Feng Y, Hsu FC, Lu YT, Lin YF, Lin CT, Lin CF, Lu YC, Liang SY (2020) Temperature prediction of ultrasonic vibration-assisted milling. *Ultrasonics* 108:106212. <https://doi.org/10.1016/j.ultras.2020.106212>
- Feng Y, Hsu FC, Lu YT, Lin YF, Lin CT, Lin CF, Lu YC, Liang SY (2020) Force prediction in ultrasonic vibration-assisted milling. *Mach Sci Technol* 25:307–330. <https://doi.org/10.1080/10910344.2020.1815048>
- Feng Y, Hsu FC, Lu YT, Lin YF, Lin CT, Lin CF, Lu YC, Liang SY (2020) Tool wear rate prediction in ultrasonic vibration-assisted milling. *Mach Sci Technol* 24:758–780. <https://doi.org/10.1080/10910344.2020.1752240>
- Feng Y, Hsu FC, Lu YT, Lin YF, Lin CT, Lin CF, Lu YC, Lu X, Liang SY (2020) Surface roughness prediction in ultrasonic vibration-assisted milling. *J Adv Mech Des Syst Manuf* 14:JAMDSM0063-JAMDSM0063. <https://doi.org/10.1299/jamdsm.2020jamdsm0063>
- Shen XH, Tao GC (2015) Tribological behaviors of two micro textured surfaces generated by vibrating milling under boundary lubricated sliding. *Int J Adv Manuf Technol* 79:1995–2002. <https://doi.org/10.1007/s00170-015-6965-x>
- Chen W, Zheng L, Huo D, Chen Y (2018) Surface texture formation by non-resonant vibration assisted micro milling. *J Micro-mech Microeng.* <https://doi.org/10.1088/1361-6439/aaa06f>
- Chen W, Zheng L, Xie W, Yang K, Huo D (2019) Modelling and experimental investigation on textured surface generation in vibration-assisted micro-milling. *J Mater Process Technol* 266:339–350. <https://doi.org/10.1016/j.jmatprotec.2018.11.011>
- Shen XH, Shi YL, Zhang JH, Zhang QJ, Tao GC, Bai LJ (2020) Effect of process parameters on micro-textured surface generation in feed direction vibration assisted milling. *Int J Mech Sci.* <https://doi.org/10.1016/j.ijmecsci.2019.105267>
- Lu H, Zhu L, Yang Z, Lu H, Yan B, Hao Y, Qin S (2021) Research on the generation mechanism and interference of surface texture in ultrasonic vibration assisted milling. *Int J Mech Sci.* <https://doi.org/10.1016/j.ijmecsci.2021.106681>

33. Börner R, Winkler S, Junge T, Titsch C, Schubert A, Drossel WG (2018) Generation of functional surfaces by using a simulation tool for surface prediction and micro structuring of cold-working steel with ultrasonic vibration assisted face milling. *J Mater Process Technol* 255:749–759. <https://doi.org/10.1016/j.jmatprotec.2018.01.027>
34. Zhao B, Li P, Zhao C, Wang X (2020) Fractal characterization of surface microtexture of Ti6Al4V subjected to ultrasonic vibration assisted milling. *Ultrasonics*. <https://doi.org/10.1016/j.ultras.2019.106052>
35. Guo P, Ehmann KF (2013) An analysis of the surface generation mechanics of the elliptical vibration texturing process. *Int J Mach Tools Manuf* 64:85–95. <https://doi.org/10.1016/j.ijmachtools.2012.08.003>
36. Liu X, Wu D, Zhang J, Hu X, Cui P (2019) Analysis of surface texturing in radial ultrasonic vibration-assisted turning. *J Mater Process Technol* 267:186–195. <https://doi.org/10.1016/j.jmatprotec.2018.12.021>
37. Kilic ZM, Altintas Y (2016) Generalized modelling of cutting tool geometries for unified process simulation. *Int J Mach Tools Manuf* 104:14–25. <https://doi.org/10.1016/j.ijmachtools.2016.01.007>
38. Tao G, Ma C, Bai L, Shen X, Zhang J (2016) Feed-direction ultrasonic vibration–assisted milling surface texture formation. *Mater Manuf Processes* 32:193–198. <https://doi.org/10.1080/10426914.2016.1198029>
39. Gao H, Yue C, Liu X, Nan Y (2019) Simulation of surface topography considering cut-in impact and tool flank wear. *Appl Sci*. <https://doi.org/10.3390/app9040732>
40. Zhu L, Ni C, Yang Z, Liu C (2019) Investigations of micro-textured surface generation mechanism and tribological properties in ultrasonic vibration-assisted milling of Ti–6Al–4V. *Precis Eng* 57:229–243. <https://doi.org/10.1016/j.precisioneng.2019.04.010>

Publisher's Note Springer Nature remains neutral with regard to jurisdictional claims in published maps and institutional affiliations.

Springer Nature or its licensor holds exclusive rights to this article under a publishing agreement with the author(s) or other rightsholder(s); author self-archiving of the accepted manuscript version of this article is solely governed by the terms of such publishing agreement and applicable law.